

RESEARCH ARTICLE

Open Access

# The competition between Lorentz and Coriolis forces in planetary dynamos

Krista M. Soderlund<sup>1\*</sup>, Andrey Sheyko<sup>2</sup>, Eric M. King<sup>3</sup> and Jonathan M. Aurnou<sup>4</sup>

## Abstract

Fluid motions within planetary cores generate magnetic fields through dynamo action. These core processes are driven by thermo-compositional convection subject to the competing influences of rotation, which tends to organize the flow into axial columns, and the Lorentz force, which tends to inhibit the relative movement of the magnetic field and the fluid. It is often argued that these forces are predominant and approximately equal in planetary cores; we test this hypothesis using a suite of numerical geodynamo models to calculate the Lorentz to Coriolis force ratio directly. Our results show that this ratio can be estimated by  $\Lambda_d^* \simeq \Lambda_i Rm^{-1/2}$  ( $\Lambda_i$  is the traditionally defined Elsasser number for imposed magnetic fields and  $Rm$  is the system-scale ratio of magnetic induction to magnetic diffusion). Best estimates of core flow speeds and magnetic field strengths predict the geodynamo to be in magnetostrophic balance where the Lorentz and Coriolis forces are comparable. The Lorentz force may also be significant, i.e., within an order of magnitude of the Coriolis force, in the Jovian interior. In contrast, the Lorentz force is likely to be relatively weak in the cores of Saturn, Uranus, Neptune, Ganymede, and Mercury.

**Keywords:** Planetary dynamos; Core convection; Magnetic fields; Rotation; Magnetostrophic force balance

## Background

Magnetic fields are common throughout the solar system and provide a unique perspective on the internal dynamics of planetary interiors. Planetary magnetic fields are driven by the conversion of kinetic energy into magnetic energy; this process is called dynamo action. Kinetic energy is derived from thermo-compositional convection of an electrically conducting fluid although mechanical mechanisms, such as libration and precession, may also drive core flow in smaller bodies (e.g., Le Bars et al. 2015). The geodynamo is the most studied planetary magnetic field, yet the mechanisms that control its strength, morphology, and secular variation are still not well understood. Towards explaining these observations, dimensionless parameters are often used to characterize the force balances present in the core and their link to processes that govern convective dynamics and dynamo action. Two forces that are particularly influential on core processes are the Coriolis force, which tends to organize the core

fluid motions, and the Lorentz force which back-reacts on the fluid motions to equilibrate magnetic field growth.

In order to better understand the manifestation of Coriolis and Lorentz forces on core flow, let us consider the Boussinesq momentum equation. In this commonly used approximation, the material properties are assumed to be constant and the density is treated as constant except in the buoyancy force of the momentum equation (e.g., Tritton 1998):

$$\frac{D\mathbf{u}}{Dt} + 2\boldsymbol{\Omega} \times \mathbf{u} = -\nabla\Pi - \alpha T'\mathbf{g} + \nu\nabla^2\mathbf{u} + \frac{1}{\rho_0}\mathbf{J} \times \mathbf{B}. \quad (1)$$

Here,  $\mathbf{u}$  is the velocity vector,  $\boldsymbol{\Omega}$  is the rotation rate of the reference frame,  $\Pi$  is the non-hydrostatic pressure normalized by the background density  $\rho_0$ ,  $\mathbf{J}$  is the electric current density,  $\mathbf{B}$  is the magnetic induction, and  $\mathbf{g}$  is the acceleration of gravity. Terms from left to right are inertial acceleration, Coriolis acceleration, pressure gradient, buoyancy, viscous diffusion, and Lorentz force. The inertial term consists of the temporal evolution of the velocity field as well as non-linear advection. The pressure gradient term absorbs the hydrostatic mean gravitational component as well as the centrifugal force. The buoyancy force arises from density differences with respect to the density

\*Correspondence: krista@ig.utexas.edu

<sup>1</sup>Institute for Geophysics, John A. & Katherine G. Jackson School of Geosciences, The University of Texas at Austin, J. J. Pickle Research Campus, Building 196 (ROC), 10100 Burnet Road (R2200), Austin, Texas, 78758-4445, USA  
Full list of author information is available at the end of the article

of the motionless background state (assumed to be constant density  $\rho_0$ ). These perturbations,  $\rho'/\rho_0 = -\alpha T'$ , are produced by temperature variations,  $T'$ , from the background state temperature profile;  $\alpha$  is thermal expansivity. Viscous diffusion depends on the kinematic viscosity of the fluid,  $\nu$ . The Lorentz force is due to interactions between the magnetic field and current density.

Planetary cores are rapidly rotating and the Coriolis force is expected to be large compared to the viscous, inertial, and buoyancy forces at global scales (the former two forces are scale dependent quantities). If we neglect these forces and magnetic fields in the Boussinesq momentum equation (Eq. 1), the system is in geostrophic balance:

$$2\boldsymbol{\Omega} \times \mathbf{u} = -\nabla\Pi. \quad (2)$$

This balance requires horizontal fluid motions to follow lines of constant pressure. Further insight can be obtained by taking the curl of Eq. 2 and using the continuity equation ( $\nabla \cdot \mathbf{u} = 0$ ) to obtain  $\boldsymbol{\Omega} \cdot \nabla \mathbf{u} = 0$ . If we assume  $\boldsymbol{\Omega} = \Omega \hat{\mathbf{z}}$  where  $\Omega$  is constant, this equation simplifies to

$$\frac{\partial \mathbf{u}}{\partial z} = 0. \quad (3)$$

This is the Taylor-Proudman theorem and states that the fluid motion will be invariant along the direction of the rotation axis. However, in order for convection to occur, the Taylor-Proudman constraint cannot strictly hold as there must be slight deviations from two-dimensionality, at least in the boundary layers, to allow overturning motions in the fluid layer (e.g., Zhang 1992; Olson et al. 1999; Grooms et al. 2010). Further beyond the onset of convection, convective flows break down into an anisotropic rotating turbulence (e.g., Sprague et al. 2006; Julien et al. 2012; Stellmach et al. 2014; Cheng et al. 2015; Ribeiro et al. 2015).

Linear asymptotic analyses of quasigeostrophic convection predict that the azimuthal wavenumber of these columns relative to the thickness of the fluid shell varies as  $\ell_U/D \propto E^{1/3}$ , where the Ekman number,  $E = \nu/(2\Omega D^2)$ , represents the ratio of viscous to Coriolis forces (e.g., Roberts 1968; Julien et al. 1998; Jones et al. 2000; Dormy et al. 2004). Thus, in rapidly rotating systems such as planetary cores (where  $E \lesssim 10^{-12}$ ), it is often predicted that quasigeostrophic convection occurs as tall, thin columns (e.g., Kageyama et al. 2008; cf. Cheng et al. 2015).

In planetary dynamos, however, magnetic fields are also thought to play an important dynamical role on the convection and zonal flows. When strong imposed magnetic fields and rapid rotation are both present, the dominant force balance is magnetostrophic—a balance between the Coriolis, pressure gradient, and Lorentz terms:

$$2\boldsymbol{\Omega} \times \mathbf{u} = -\nabla\Pi + \frac{1}{\rho_0} \mathbf{J} \times \mathbf{B}. \quad (4)$$

In contrast to Eq. 3, the curl of the magnetostrophic balance Eq. 4 yields

$$\frac{\partial \mathbf{u}}{\partial z} = -\frac{1}{2\rho_0\Omega} \nabla \times (\mathbf{J} \times \mathbf{B}). \quad (5)$$

This equation shows that magnetic fields can relax the Taylor-Proudman constraint, allowing global-scale motions that differ fundamentally from the small-scale axial columns typical of non-magnetic, rapidly rotating convection (e.g., Cardin and Olson 1995; Olson and Glatzmaier 1996; Zhang and Schubert 2000; Roberts and King 2013).

Magnetic fields are typically considered to be important dynamically when the ratio of Lorentz to Coriolis forces is of order unity. This ratio is represented by the Elsasser number,  $\Lambda$ , which can be approximated by assuming a characteristic current density, magnetic induction, density, rotation rate, and velocity scale:

$$\Lambda = \frac{\text{Lorentz}}{\text{Coriolis}} = \frac{\left| \frac{1}{\rho_0} \mathbf{J} \times \mathbf{B} \right|}{|2\boldsymbol{\Omega} \times \mathbf{u}|} \approx \frac{JB}{2\rho_0\Omega U}. \quad (6)$$

In systems where the magnetic field is not strongly time variant (i.e.,  $\partial \mathbf{B}/\partial t = -\nabla \times \mathbf{E} \sim 0$ ), the current density can be approximated via Ohm's Law,  $J \sim \sigma UB$  where  $\sigma = (\mu_0\eta)^{-1}$  is electrical conductivity and  $\eta$  is magnetic diffusivity, such that

$$\Lambda_i = \frac{B^2}{2\rho_0\mu_0\eta\Omega}. \quad (7)$$

This formulation is thus appropriate for steady *imposed* magnetic fields (e.g., Olson and Glatzmaier 1996; King and Aurnou 2015). In dynamos, which tend to exhibit significant temporal variability, it is more appropriate to approximate the current density using Ampere's law under the MHD approximation,  $J \sim B/\mu_0\ell_B$  where  $\ell_B$  is the characteristic length scale of magnetic field variations (e.g., Cardin et al. 2002; Soderlund et al. 2012). In this *dynamic* case, Eq. 6 becomes

$$\Lambda_d = \frac{B^2}{2\rho_0\mu_0\Omega U \ell_B} = \frac{\Lambda_i}{Rm} \frac{D}{\ell_B}, \quad (8)$$

indicating that the Lorentz to Coriolis force ratio is length scale dependent. In the latter equality,  $Rm = UD/\eta$  is the global ratio of magnetic induction to magnetic diffusion. This parameter must exceed approximately 10 in order for dynamo action to occur (e.g., Roberts 2007). Thus, on global scales, where  $\ell_B \simeq D$ , the dynamic Elsasser number will always be less than  $\Lambda_i$  by at least an order of magnitude for active dynamos. However, the influence of magnetic fields will become increasingly important at smaller scales since  $\Lambda_d \propto \ell_B^{-1}$  in (Eq. 8).

The quantity  $\ell_B/D$  cannot be measured for planetary cores, however. It is, therefore, important to provide a scaling estimate for  $\Lambda_d$  in terms of quantities that can

be estimated from observations, such as  $\Lambda_i$  and  $Rm$ . The length scale  $\ell_B$  can be approximated using the magnetic induction equation:

$$\frac{\partial \mathbf{B}}{\partial t} = \nabla \times (\mathbf{u} \times \mathbf{B}) + \eta \nabla^2 \mathbf{B} \quad (9)$$

Assuming a balance between induction and diffusion yields  $UB/D \sim \eta B/\ell_B^2$ . Rearranging, the dimensionless length scale is proportional to the inverse square root of the magnetic Reynolds number:

$$\ell_B/D \sim Rm^{-1/2} \quad (10)$$

(e.g., Galloway 1978; King and Roberts 2013). Using this relationship in Eq. 8, we estimate the dynamic Lorentz to Coriolis force ratio to be

$$\Lambda_d^* \sim \Lambda_i Rm^{-1/2}. \quad (11)$$

This scaling estimate will be referred to as the *modified dynamic* Elsasser number.

In this paper, we will investigate the relative magnitudes of Lorentz and Coriolis forces to better understand the dynamics of planetary cores. Towards this end, we calculate directly the Lorentz to Coriolis force ratio in a suite of geodynamo models described in the ‘‘Methods’’ section, test Eq. 11 to predict this ratio in the ‘‘Results’’ section, and extrapolate the results to Earth and other planetary cores in the ‘‘Discussion’’ section.

## Methods

We analyze 34 dynamo models presented in Soderlund et al. (2012, 2014) and five dynamo models presented in Sheyko (2014); these datasets will be referred to as SKA and S14, respectively. These simulations of Boussinesq convection and dynamo action are carried out in thick, rotating spherical shells with thickness  $D$ , rotation rate  $\Omega$ , and no-slip boundaries. Gravity is assumed to vary linearly with radius;  $g_o$  is acceleration at the top of the fluid shell. The outer boundary at radius  $r_o$  is assumed electrically insulating and the solid inner core at radius  $r_i$  has the same electrical conductivity as the convecting fluid region.

The SKA dataset considers three rotation rates (Ekman numbers in the range  $10^{-3} \geq E \geq 10^{-5}$ ), two magnetic diffusivities (magnetic Prandtl numbers of  $Pm = 2, 5$ ), and thermal forcing near onset ( $Ra_c$ ) to more than 1000 times critical ( $1.9 < Ra/Ra_c < 1125$ ); the shell geometry is fixed to  $\chi = r_i/r_o = 0.4$  with isothermal boundaries. This survey is complemented by the S14 dataset focusing on low Ekman, low magnetic Prandtl number simulations:  $3 \times 10^{-7} \lesssim E \lesssim 10^{-6}$ ,  $0.05 \leq Pm \leq 1$ , and  $10^8 \lesssim Ra \lesssim 10^{10}$  with  $\chi = 0.35$ , an isothermal inner shell boundary, and fixed heat flux on the outer shell boundary. For both datasets, the thermal ( $\kappa$ ) and momentum ( $\nu$ ) diffusivities are assumed equal, such that the Prandtl number,

$Pr = \nu/\kappa$ , is unity. Here,  $E = \nu/(2\Omega D^2)$  is the ratio of viscous to Coriolis forces;  $Pm = \nu/\eta$  is the ratio of viscous to magnetic diffusivities, and  $Ra = \alpha g_o \Delta T D^3/(\nu\kappa)$  is the ratio of buoyancy due to superadiabatic temperature contrast  $\Delta T$  to diffusion. The combination of these datasets, given in Table 1, results in one of the broadest surveys of supercriticality, Ekman, and magnetic Prandtl numbers in the literature.

The SKA simulations are carried out on numerical grids that range from 37 fluid shell radial levels and 42 spherical harmonic degrees (near onset at  $E = 10^{-3}$ ) to 73 radial levels and 213 spherical harmonic degrees (highest  $Ra$  for  $E = 10^{-5}$ ). Hyperdiffusion is used for the three most extreme cases ( $Ra \geq 2 \times 10^8$  for  $E \leq 10^{-4}$ ); additional details are given in Soderlund et al. (2012). The S14 simulations are carried out on numerical grids with 512–528 radial levels and 256 spherical harmonic degrees. All simulations are carried out using pseudo-spectral methods with no azimuthal symmetries assumed (Wicht 2002; Christensen and Wicht, 2007; Sheyko 2014). Once the initial transient has subsided, global diagnostic quantities ( $\Lambda_i$ ,  $Rm$ ,  $\ell_B$ ,  $\Lambda_d$ , and  $\Lambda_d^*$ ) are time-averaged to minimize statistical errors.

In our models, the imposed Elsasser number is calculated from the dimensionless magnetic energy density,  $\mathcal{E}_M$ , within the fluid shell of volume  $V$ :

$$\Lambda_i = 2PmE\mathcal{E}_M \text{ where } \mathcal{E}_M = \frac{1}{2PmEV} \int_V \mathbf{B} \cdot \mathbf{B} dV, \quad (12)$$

while the magnetic Reynolds number is calculated from the dimensionless kinetic energy density,  $\mathcal{E}_K$ :

$$Rm = \sqrt{2\mathcal{E}_K}Pm \text{ where } \mathcal{E}_K = \frac{1}{2V} \int_V \mathbf{u} \cdot \mathbf{u} dV. \quad (13)$$

These quantities are non-dimensionalized using distance, magnetic induction, velocity, and energy density scales of  $D = r_o - r_i$ ,  $\sqrt{2\rho\mu_o\eta\Omega}$ ,  $\nu/D$ , and  $\rho\nu^2/D^2$ , respectively. We also characterize  $\ell_B$  as a quarter wavelength of the typical magnetic field wavenumber (Soderlund et al. 2012):

$$\ell_B/D \sim \frac{(\pi/2)}{\sqrt{\bar{l}_B^2 + \bar{m}_B^2}}, \text{ where } \bar{l}_B = \frac{\sum l(\mathbf{B}_l \cdot \mathbf{B}_l)}{2PmE\mathcal{E}_M} \text{ and } \bar{m}_B = \frac{\sum m(\mathbf{B}_m \cdot \mathbf{B}_m)}{2PmE\mathcal{E}_M}. \quad (14)$$

Here,  $\mathbf{B}_l$  and  $\mathbf{B}_m$  are magnetic induction at spherical harmonic degree  $l$  and order  $m$ .

Two approaches are used to calculate the Lorentz to Coriolis force ratio in situ. The first integrates the Lorentz

**Table 1** Input ( $E, Pm, Ra, Ro_c = \sqrt{RaE^2/Pr}$ ) and output ( $\Lambda_i, \Lambda_d, \Lambda_d^*, \Lambda^I, \Lambda^P$ ) parameters for our dataset.  $Pr = 1$  is fixed for all simulations. Additional simulation information is given in Soderlund et al. (2012, 2014) for cases with  $E \geq 10^{-5}$  and Sheyko (2014) for cases with  $E \lesssim 10^{-6}$

$E$	$Pm$	$Ra$	$Ro_c$	$\Lambda_i$	$\Lambda_d$	$\Lambda_d^*$	$\Lambda^I$	$\Lambda^P$
$10^{-3}$	5	$6.50 \times 10^4$	0.26	4.34	0.44	0.47	0.39	0.26
$10^{-3}$	5	$9.70 \times 10^4$	0.31	3.91	0.30	0.35	0.43	0.32
$10^{-3}$	5	$1.12 \times 10^5$	0.33	3.25	0.20	0.25	0.40	0.29
$10^{-3}$	5	$1.32 \times 10^5$	0.36	0.61	0.03	0.04	0.05	0.01
$10^{-3}$	5	$5.00 \times 10^5$	0.71	4.14	0.15	0.17	0.29	0.16
$10^{-3}$	5	$1.96 \times 10^6$	1.40	23.0	0.51	0.64	0.79	0.46
$10^{-3}$	5	$1.96 \times 10^7$	4.43	248	2.62	4.00	4.20	3.12
$10^{-4}$	2	$1.42 \times 10^6$	0.12	1.30	0.14	0.12	0.18	0.12
$10^{-4}$	2	$2.12 \times 10^6$	0.15	2.10	0.17	0.16	0.21	0.14
$10^{-4}$	2	$2.83 \times 10^6$	0.17	2.42	0.17	0.16	0.24	0.16
$10^{-4}$	2	$3.54 \times 10^6$	0.19	2.37	0.15	0.14	0.27	0.19
$10^{-4}$	2	$3.68 \times 10^6$	0.19	2.36	0.15	0.13	0.21	0.17
$10^{-4}$	2	$3.75 \times 10^6$	0.19	2.27	0.14	0.12	0.21	0.15
$10^{-4}$	2	$3.82 \times 10^6$	0.20	0.14	0.01	0.007	0.01	0.006
$10^{-4}$	2	$3.96 \times 10^6$	0.20	0.18	0.01	0.009	0.02	0.009
$10^{-4}$	2	$4.11 \times 10^6$	0.20	0.22	0.01	0.01	0.02	0.009
$10^{-4}$	2	$4.24 \times 10^6$	0.21	0.24	0.02	0.01	0.02	0.006
$10^{-4}$	2	$6.00 \times 10^6$	0.24	0.68	0.04	0.03	0.06	0.03
$10^{-4}$	2	$8.50 \times 10^6$	0.29	1.53	0.07	0.06	0.11	0.06
$10^{-4}$	2	$1.42 \times 10^7$	0.38	3.44	0.13	0.11	0.21	0.11
$10^{-4}$	2	$2.10 \times 10^7$	0.46	5.48	0.18	0.16	0.28	0.17
$10^{-4}$	2	$4.24 \times 10^7$	0.65	11.4	0.29	0.26	0.44	0.27
$10^{-4}$	2	$8.00 \times 10^7$	0.89	20.7	0.40	0.39	0.59	0.37
$10^{-4}$	2	$1.42 \times 10^8$	1.19	36.3	0.58	0.58	0.81	0.53
$10^{-4}$	2	$4.24 \times 10^8$	2.06	106	0.84	1.28	1.18	0.77
$10^{-4}$	2	$8.48 \times 10^8$	2.91	197	1.11	2.10	1.63	1.07
$10^{-5}$	2	$3.10 \times 10^7$	0.06	4.84	0.30	0.30	0.39	0.33
$10^{-5}$	2	$5.89 \times 10^7$	0.08	7.07	0.31	0.31	0.45	0.37
$10^{-5}$	2	$8.20 \times 10^7$	0.09	8.28	0.32	0.30	0.45	0.34
$10^{-5}$	2	$8.50 \times 10^7$	0.09	8.54	0.32	0.31	0.47	0.39
$10^{-5}$	2	$9.50 \times 10^7$	0.10	9.02	0.32	0.30	0.45	0.35
$10^{-5}$	2	$1.05 \times 10^8$	0.10	9.63	0.33	0.31	0.47	0.34
$10^{-5}$	2	$1.50 \times 10^8$	0.12	12.4	0.36	0.35	0.52	0.37
$10^{-5}$	2	$2.00 \times 10^8$	0.14	14.8	0.38	0.37	0.56	0.36
$1.2 \times 10^{-6}$	1	$1.86 \times 10^8$	0.02	5.73	0.21	0.28	0.39	0.30
$1.2 \times 10^{-6}$	0.2	$1.86 \times 10^8$	0.04	0.07	0.005	0.007	0.01	0.009
$1.2 \times 10^{-6}$	0.2	$9.28 \times 10^8$	0.09	0.61	0.03	0.03	0.08	0.04
$1.2 \times 10^{-6}$	0.2	$5.57 \times 10^9$	0.02	9.92	0.24	0.25	0.47	0.30
$3.0 \times 10^{-7}$	0.05	$2.23 \times 10^{10}$	0.04	3.61	0.13	0.17	0.32	0.24

( $\mathbf{F}_L$ ) and Coriolis ( $\mathbf{F}_C$ ) forces over the spherical shell volume following Soderlund et al. (2012):

$$F_L^I = \int_V \left( (\mathbf{F}_L \cdot \hat{\mathbf{r}})^2 + (\mathbf{F}_L \cdot \hat{\theta})^2 + (\mathbf{F}_L \cdot \hat{\phi})^2 \right)^{1/2} dV \quad (15)$$

$$F_C^I = \int_V \left( (\mathbf{F}_C \cdot \hat{\mathbf{r}})^2 + (\mathbf{F}_C \cdot \hat{\theta})^2 + (\mathbf{F}_C \cdot \hat{\phi})^2 \right)^{1/2} dV \quad (16)$$

where the volume-integrated force ratio is  $\Lambda^I = F_L^I/F_C^I$ . Alternatively, the root mean square (RMS) Lorentz and Coriolis forces are calculated at each grid point to determine the force ratio locally (cf. Dharmaraj and Stanley 2012; Dharmaraj et al. 2014). A representative value is determined by taking the most probable ratio in the histogram; this *probability* approach yields  $\Lambda^P$  (Fig. 1). Histogram bins are uniformly spaced to contain equal ranges of  $\log_{10}(F_L^{RMS}/F_C^{RMS})$  values. The probability of each bin is defined as the volume of the fluid shell that is occupied by the respective range of force ratio values relative to the total volume of the fluid shell. For both approaches, velocity and magnetic fields from three random snapshots in time are used to calculate the force ratios for the SKA dataset, with  $\Lambda^I$  and  $\Lambda^P$  being the average values. Single snapshots are used for the S14 dataset.

## Results

A Lorentz to Coriolis force ratio histogram is evaluated for a representative dipole-dominated dynamo case at a snapshot in time in Fig. 1. The histogram indicates that the

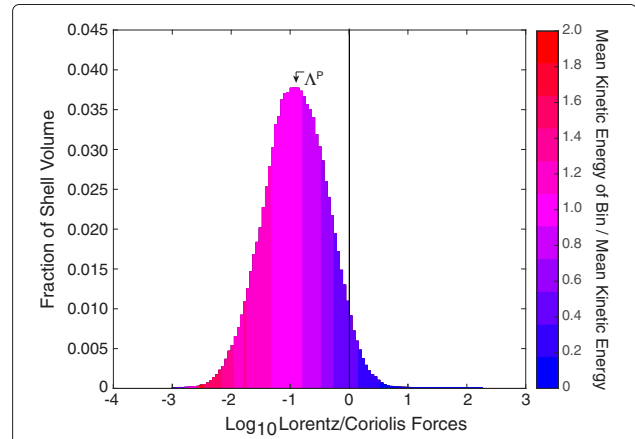


**Fig. 1** Histogram of Lorentz to Coriolis force ratios on a point-by-point basis. Histogram showing the distribution of Lorentz to Coriolis forces at each point in our simulation with  $E = 10^{-4}$ ,  $Ra = 1.9Ra_c$ ,  $Pr = 1$ , and  $Pm = 2$ . Color denotes the mean kinetic energy per force ratio bin relative to the mean kinetic energy of the system. The probability Elsasser number corresponds to the most probable force ratio bin,  $\Lambda^P = 0.12$ . In contrast, the imposed Elsasser number is  $\Lambda_i = 1.31$ , the integrated Elsasser number is  $\Lambda^I = 0.18$ , the dynamic Elsasser number is  $\Lambda_d = 0.14$ , and the modified dynamic Elsasser number is  $\Lambda_d^* = 0.12$

Coriolis force is dominant for the majority of grid points, most frequently by an order of magnitude. Moreover, the points with Lorentz to Coriolis force ratios greater than unity tend to have relatively low kinetic energies, denoted by coloration of the bins. Thus, the Lorentz force is expected to have a secondary influence on the convective (non-zonal) dynamics (Soderlund et al. 2012). This does not mean, however, that the magnetic field cannot have an important, local-scale dynamical impact (cf. Sreenivasan and Jones 2011).

Figure 2 shows the ratio of Lorentz to Coriolis forces in our simulations as characterized by the *integrated*  $\Lambda^I$ , *probability*  $\Lambda^P$ , *imposed*  $\Lambda_i$ , *dynamic*  $\Lambda_d$ , and *modified dynamic*  $\Lambda_d^*$  Elsasser numbers (see Table 2 for a summary

of definitions). For comparison, ratios of these parameters are plotted in Fig. 3. The  $\Lambda_i$  Elsasser number, which is traditionally used to test for magnetostrophic balance, substantially overestimates the Lorentz to Coriolis force ratio in all of our dynamo models (i.e., typically by an order of magnitude; see Fig. 3a). In contrast, we find that all of the other Lorentz to Coriolis force ratio definitions ( $\Lambda^I$ ,  $\Lambda^P$ ,  $\Lambda_d$ ,  $\Lambda_d^*$ ) agree to within a factor of five; a factor of 1.4 is the mean deviation between definitions. Comparing the in situ calculations,  $\Lambda^I$  exceeds  $\Lambda^P$  in all cases investigated. This result implies that, independent of the Ekman and magnetic Prandtl numbers and in agreement with the literature (e.g., Aubert et al. 2008, Sreenivasan et al. 2014), the Lorentz force is concentrated in discrete regions that

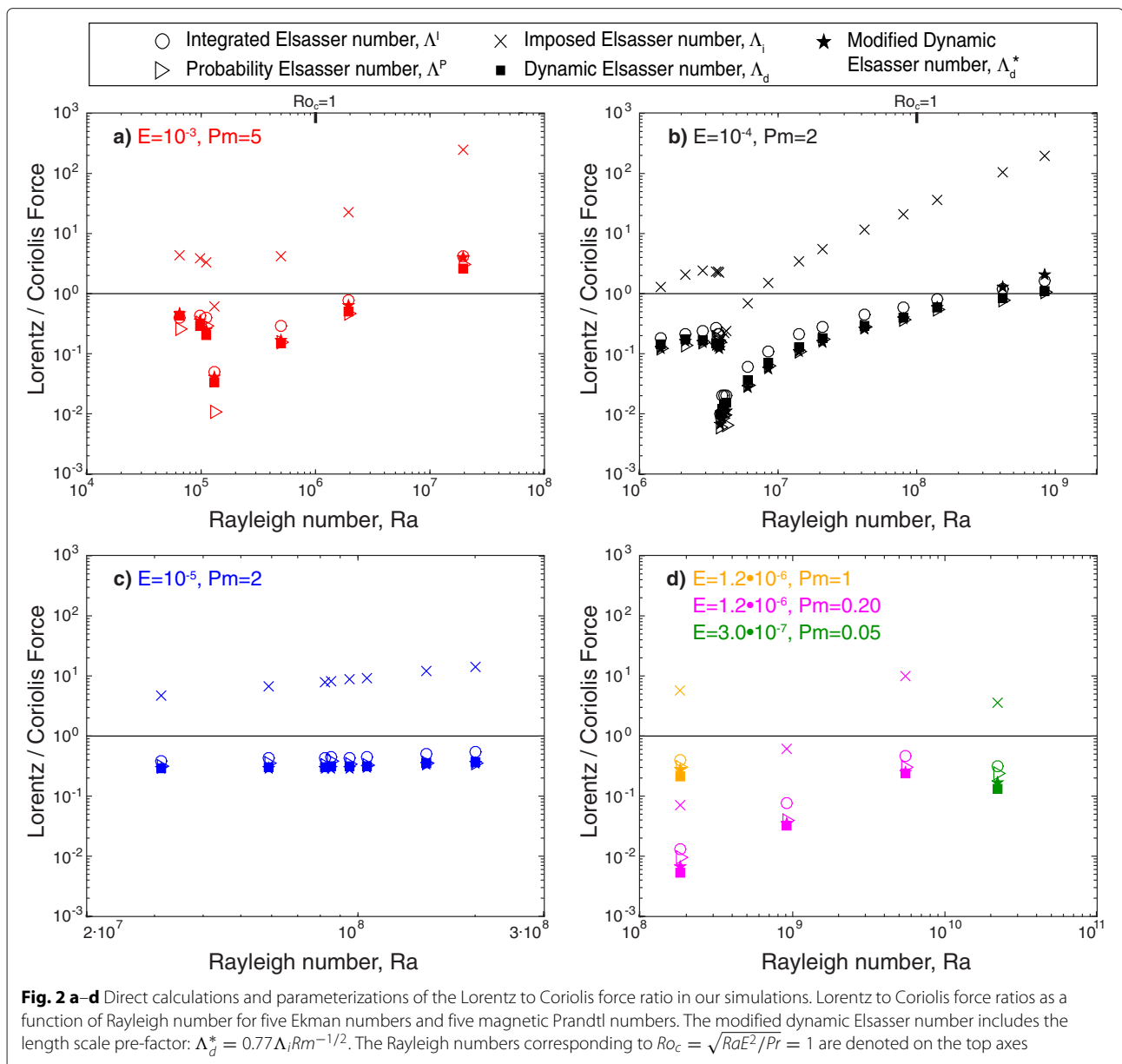


**Table 2** Elsasser number definitions: (1) Imposed  $\Lambda_i$ , (2) Dynamic  $\Lambda_d$ , (3) Modified dynamic  $\Lambda_d^*$ , (4) Integrated  $\Lambda^I$ , and (5) Probability  $\Lambda^P$

$\Lambda_i$	$\Lambda_d$	$\Lambda_d^*$	$\Lambda^I$	$\Lambda^P$
$\frac{B^2}{2\rho_0\mu_0\eta\Omega}$	$\frac{\Lambda_i D}{Rm \ell_B}$	$0.77 \frac{\Lambda_i}{Rm^{1/2}}$	$\frac{\int_V  \mathbf{F}_L  dV}{\int_V  \mathbf{F}_C  dV}$	$\frac{ \mathbf{F}_L }{ \mathbf{F}_C }$ , max probability

are more influenced by magnetic fields than the rest of the fluid volume. Similarly, the dynamic Elsasser number is also found to be in better agreement with  $\Lambda^P$  than  $\Lambda^I$  (Fig. 3b, c); the mean (maximum) percent differences between  $\Lambda_d$  and  $\Lambda^P$  are 28 % (68 %) for  $E = 10^{-3}$ , 18 % (58 %) for  $E = 10^{-4}$ , 9 % (21 %) for  $E = 10^{-5}$ , and 49 % (80 %) for  $E \lesssim 10^{-5}$ .

The Lorentz to Coriolis force ratios in Fig. 2 have distinct minima for cases with  $E \geq 10^{-4}$ . This sharp drop as the Rayleigh number is increased from onset occurs when the dipole-dominance of the dynamo breaks down. The Lorentz force increases more rapidly than the Coriolis force as  $Ra$  is further increased (see Fig. 4a of Soderlund et al. 2012), which explains the subsequent increase in Elsasser numbers.

Before discussing the modified Elsasser number, the assumption that the dimensionless length scale representative of magnetic field gradients in our simulations is approximately equal to the theoretical prediction (Eq. 10) must be assessed. This comparison is made in Fig. 4. Agreement within a factor of two—and typically much less, 16 % difference on average—between the  $\ell_B/D$  values calculated directly from our simulations and the scaling estimate occurs when a pre-factor of 1.3 is included in Eq. 10:

$$\ell_B/D = 1.3Rm^{-1/2}. \tag{17}$$

This pre-factor is determined by minimizing the least squares residual between the calculated and predicted values across our dataset. Roberts and King (2013) also investigated the length scale of magnetic field variations in geodynamo models and found a similar dependence on  $Rm^{-1/2}$  with a pre-factor of 3 due to their slightly modified definition of  $\ell_B/D$ . More importantly, they also show that the magnetic length scale is weakly dependent on the magnetic field strength  $\Lambda_i$ , which may explain some of the spread in our model-prediction deviations.

The modified dynamic Elsasser number is given by solid, starred markers in Fig. 2; here,  $\Lambda_d^*$  has been modified compared to Eq. 11 to include the pre-factor derived from the length scale calculations (Eq. 17):

$$\Lambda_d^* = 0.77\Lambda_i Rm^{-1/2}. \tag{18}$$

For all Ekman numbers, the dynamic  $\Lambda_d$  and modified dynamic  $\Lambda_d^*$  Elsasser numbers differ by less than a factor

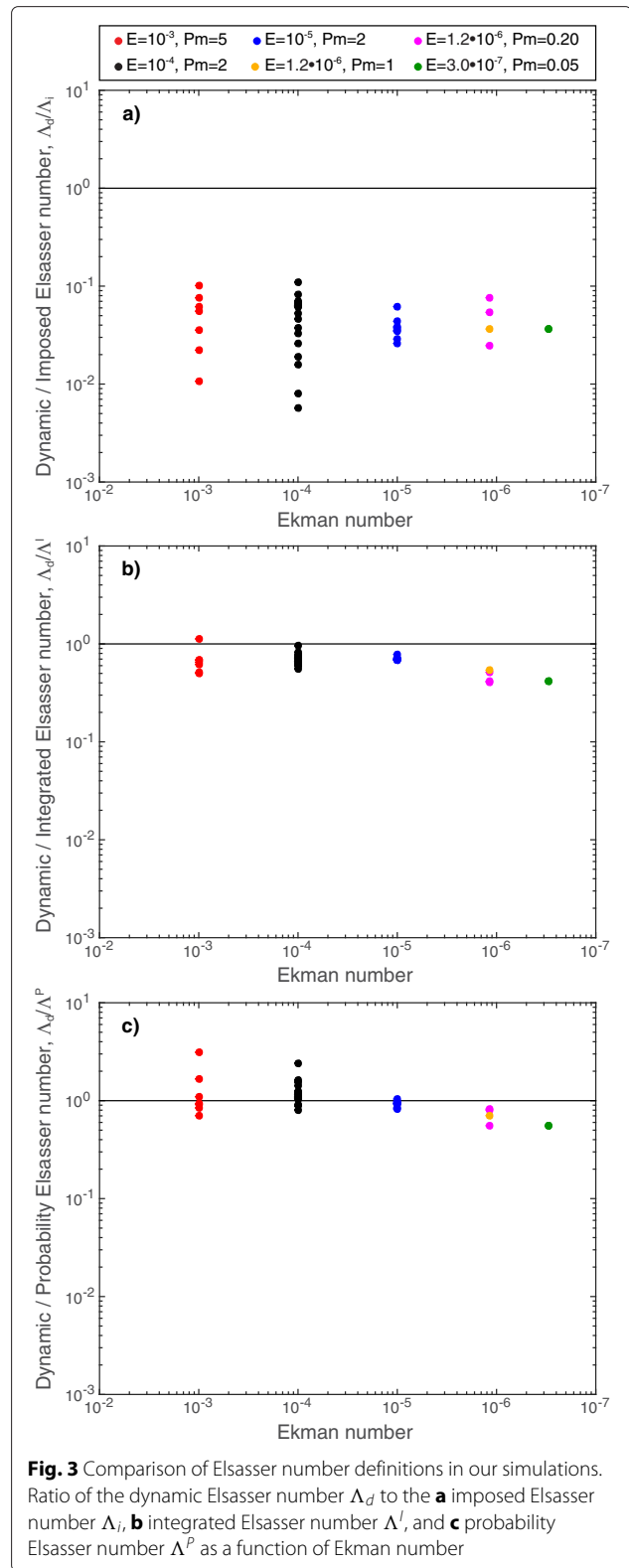


**Fig. 3** Comparison of Elsasser number definitions in our simulations. Ratio of the dynamic Elsasser number  $\Lambda_d$  to the **a** imposed Elsasser number  $\Lambda_i$ , **b** integrated Elsasser number  $\Lambda^I$ , and **c** probability Elsasser number  $\Lambda^P$  as a function of Ekman number

of two (Fig. 5): the mean (maximum) percent difference is 23 % (53 %) for  $E = 10^{-3}$ , 21 % (89 %) for  $E = 10^{-4}$ , 4 % (6 %) for  $E = 10^{-5}$ , and 19 % (30 %) for

$E \lesssim 10^{-6}$ . The differences between  $\Lambda_d^*$  and the probability Elsasser number  $\Lambda^P$  tend to be comparable: 28 % (73 %) for  $E = 10^{-3}$ , 16 % (49 %) for  $E = 10^{-4}$ , 13 % (28 %) for  $E = 10^{-5}$ , and 25 % (43 %) for  $E \lesssim 10^{-6}$ . Thus, the modified dynamic Elsasser number  $\Lambda_d^*$  accurately captures the ratio of Lorentz to Coriolis forces in our suite of simulations.

In order to apply the modified dynamic Elsasser number to planetary cores, its applicability to core conditions must first be evaluated. Our datasets cover a broad range of diagnostic physical parameters: magnetic field strengths of  $10^{-1} \lesssim \Lambda_i \lesssim 10^2$ , magnetic induction to diffusion ratios of  $10^2 \lesssim Rm \lesssim 10^4$ , and Lorentz to Coriolis force ratios of  $10^{-2} \lesssim \Lambda_d \lesssim 1$ . However, these ranges span only a fraction of the planetary parameter estimates, which vary over  $10^{-5} \lesssim \Lambda_i \lesssim 10^{10}$ ,  $10^2 \lesssim Rm \lesssim 10^5$ , and  $10^{-6} \lesssim \Lambda_d^* \lesssim 10^7$  as detailed in the “Discussion” section. The most fundamental deviation is for  $\Lambda_d > 1$ , which implies a different dominant force balance. While our dataset includes cases with  $\Lambda_d > 1$ , these simulations are strongly driven with inertia exceeding both Lorentz and Coriolis forces (see Fig. 4 of Soderlund et al. 2012), which is not expected for most planets (cf. Soderlund et al. 2013).

Figure 5 shows the ratio of the dynamic to modified dynamic Elsasser numbers as a function of the convective Rossby number,  $Ro_c = (RaE^2/Pr)^{1/2}$ , which characterizes the ratio of buoyancy-driven inertial forces to Coriolis forces (e.g., Gilman 1977, Aurnou et al. 2007). The  $\Lambda_d^*$  approximation works well when the Coriolis force dominates; in contrast, the largest discrepancy occurs when  $Ro_c > 1$ . Geodynamo simulations from Dormy (2014) provide a  $\Lambda_d^*$  test for cases with  $\Lambda_d > 1$  and  $Ro_c < 1$  at an Ekman number of  $E = 1.5 \times 10^{-4}$  and a Prandtl number of unity. Here, large magnetic Prandtl numbers ( $Pm \geq 12$ ) are required to obtain dynamo action since the inertial forces are relatively weak (i.e., quasi-laminar flows). Application of Eq. 18 to his dataset yields  $0.85 \leq \Lambda_d/\Lambda_d^* \leq 1.3$ , implying that our results are applicable to strong field systems with dominant Lorentz forces.

A discrepancy between input parameters also exists between the simulations and planetary cores. In particular, all numerical dynamo models are necessarily limited to massively overestimated kinematic viscosities, which prohibits simulations with realistic Ekman and magnetic Prandtl numbers:  $10^{-19} \lesssim E \lesssim 10^{-12}$  and  $10^{-8} \lesssim Pm \lesssim 10^{-6}$  are estimated for planets with active dynamos (e.g., Schubert and Soderlund 2011). In contrast, our dataset considers  $10^{-7} \lesssim E \lesssim 10^{-3}$  and  $10^{-1} \lesssim Pm \lesssim 10^1$ . Importantly, no clear Ekman or magnetic Prandtl number dependence is identified in Fig. 5. We, therefore, hypothesize that the modified dynamic Elsasser number (Eq. 18) can be extrapolated to extreme planetary parameters.

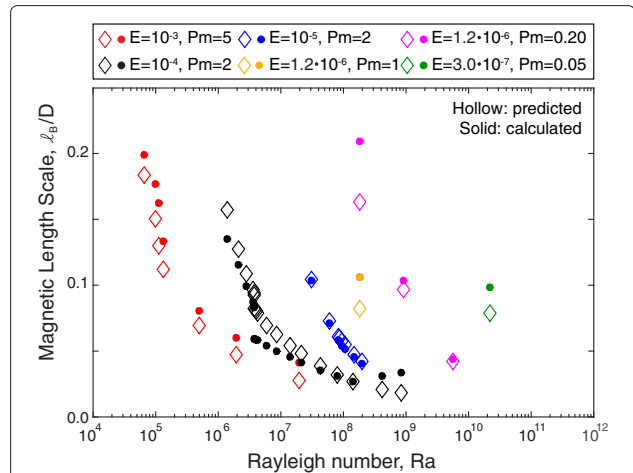


**Fig. 4** Calculated and predicted magnetic length scales. Magnetic length scale as a function of the Rayleigh number with Ekman and magnetic Prandtl numbers denoted by color. A best-fit between the calculated and predicted values is obtained when a pre-factor is included in (Eq. 10):  $\ell_B/D = 1.3Rm^{-1/2}$  (included here)

### Discussion

The modified dynamic Elsasser number can be used to estimate the Lorentz to Coriolis force ratio in planetary cores when  $\Lambda_i$  and  $Rm$  are known (see Fig. 6 and Table 3). The imposed Elsasser number is traditionally used to quantify magnetic field strengths of planets since the poloidal component ( $B_p$ ) can be measured by spacecraft and estimates for the other components (density  $\rho$ , magnetic diffusivity  $\eta$ , and rotation rate  $\Omega$ ) are relatively

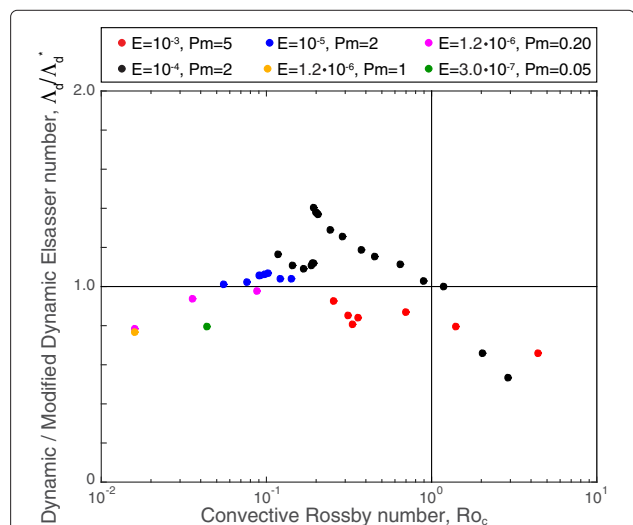


**Fig. 5** Comparison of predicted and calculated Elsasser numbers as a function of the relative strengths of buoyancy and Coriolis forces. Ratio of  $\Lambda_d/\Lambda_d^*$  plotted versus the convective Rossby number,  $Ro_c = \sqrt{RaE^2/Pr}$

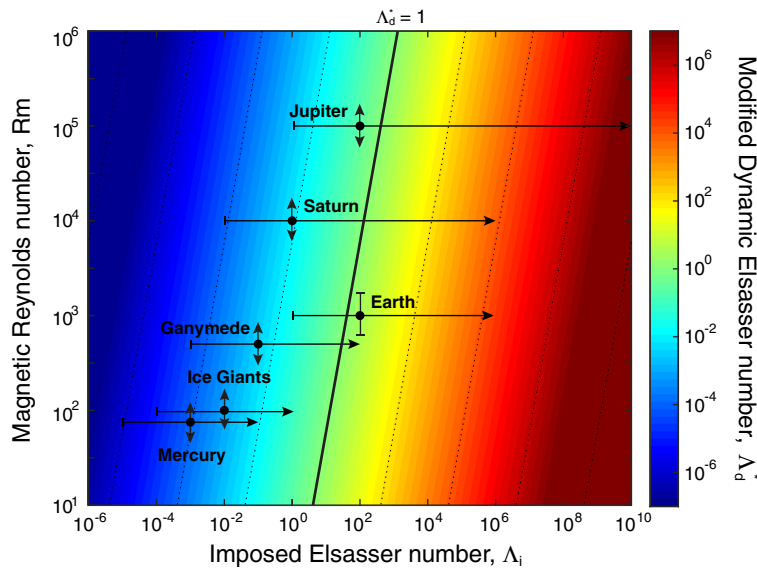


**Fig. 6** Lorentz to Coriolis force ratio predictions for planetary cores. Modified dynamic Elsasser number as a function of imposed Elsasser number and magnetic Reynolds number across a range of values that may be relevant to planets in our solar system as well as exoplanets. The approximate ranges of anticipated  $\Lambda_i$  and  $Rm$  values are given for planets with active dynamos. *Barred line ends* for  $\Lambda_i$  denote the observed magnetic field strengths; *arrowed line ends* denote upper bounds. *Barred line ends* for  $Rm$  denote constrained bounds; *arrowed line ends* denote a larger range of uncertainties. Black circles denote the most probable  $\Lambda_i$  and  $Rm$  values

straightforward (see Schubert and Soderlund 2011 for a review); these measurements constitute a lower bound since the toroidal component is not included and small-scale poloidal contributions are below the resolution of detection. Toroidal magnetic fields ( $B_T$ ) can be amplified by stretching of the poloidal field due to azimuthal differential rotation (zonal flows). This so-called  $\omega$ -effect can generate toroidal magnetic fields up to  $B_T \sim RmB_p$  (Roberts 2007), which sets an  $\Lambda_i$  upper bound. For a best estimate, we assume the total core field strength  $B$  to be an order of magnitude larger than the direct measurements (i.e.,  $\Lambda_i$  increases by a factor of 100). This assumption is motivated both by geomagnetic data (e.g., Shimizu et al. 1998) and geodynamo modeling results (e.g., Aubert et al. 2009).

**Earth:** Geodynamo core flow inversions based on secular variation of the magnetic field imply velocities of  $U \sim 5 \times 10^{-4}$  m/s (e.g., Holme 2007; Aubert 2013), which corresponds to  $Rm \sim 10^3$  assuming  $\eta \sim 1$  m<sup>2</sup>/s for liquid

metals. Ensemble inversions further suggest RMS magnetic field strengths in the cylindrical direction of  $B_S \sim 2$  mT (Gillet et al. 2010), while toroidal magnetic field constraints of  $1 < B_T/B_S < 100$  have been inferred by Shimizu et al (1998). Thus,  $B \sim 10B_S \sim 20$  mT appears to be a reasonable estimate of the core’s total field strength such that  $\Lambda_i \sim 10^2$ . In contrast, direct magnetic field measurements suggest a lower bound of  $\Lambda_i \sim 1$  and application of the  $\omega$ -effect suggests an upper bound of  $\Lambda_i \sim 10^6$ . We, therefore, predict a Lorentz to Coriolis force ratio of  $\Lambda_d^* \sim 1$  for the geodynamo, with a possible range of  $10^{-2} \lesssim \Lambda_d^* \lesssim 10^4$ . This result suggests that the Lorentz force cannot be neglected dynamically in the core and, more likely, that the core is in magnetostrophic balance.

**Mercury and Ganymede:** No observation-based velocity constraints are available currently for Mercury or Ganymede, so dynamo models that capture many of their magnetic field characteristics may serve as a basis for determining the magnetic Reynolds number. For example, Cao et al. (2014) obtain a Mercury-like dynamo when convection is driven by volumetrically distributed buoyancy sources and the core-mantle boundary heat flux peaks at low latitudes; their best fitting case has  $Rm = 75$ . Similarly, Christensen (2015) find Ganymede-like dynamos driven by iron snow with a stably stratified layer below the outer shell boundary;  $Rm \approx 500$  in his optimal simulation. Using the upper and lower bound constraints derived from the  $\omega$ -effect and observations, respectively, the imposed Elsasser number is estimated to vary between

**Table 3** Order of magnitude estimates of the magnetic Reynolds number  $Rm$ , the imposed Elsasser number  $\Lambda_i$ , and the Lorentz to Coriolis force ratio as estimated by  $\Lambda_d^*$  for planetary cores with active dynamos

	Mercury	Earth	Ganymede	Jupiter	Saturn	Ice Giants
$Rm$	75	$10^3$	500	$10^5$	$10^4$	$10^2$
$\Lambda_i$	$10^{-3}$	$10^2$	$10^{-1}$	$10^2$	$10^0$	$10^{-2}$
$\Lambda_d^*$	$10^{-4}$	$10^0$	$10^{-3}$	$10^{-1}$	$10^{-2}$	$10^{-3}$



$\Lambda_i \sim 10^{-5}$  and  $\sim 10^{-1}$  for Mercury, which corresponds to  $\Lambda_d^* \lesssim 10^{-2}$  and implies that magnetostrophic balance is unlikely in the Hermian core. Conversely, the possible magnetic field strengths for Ganymede range from  $\Lambda_i \sim 10^{-3}$  to  $\sim 10^2$ , yielding  $10^{-5} \lesssim \Lambda_d^* \lesssim 1$ . However, the best estimate for the imposed Elsasser number is  $\Lambda_i \sim 10^{-1}$  such that  $\Lambda_d^* \sim 10^{-3}$ . As a result, magnetostrophic balance is possible, but unlikely, in Ganymede's core.

**Gas Giants:** Jovian velocities can be estimated through scaling arguments and potentially secular variation. Jones (2014) suggests flow velocities of  $U \gtrsim 10^{-3}$  m/s, leading to values of  $Rm \gtrsim 10^5$  given the planet's large size. In this case, magnetic field strengths range from  $\Lambda_i \sim 1$  via core field measurements to  $\Lambda_i \sim 10^{10}$  when the  $\omega$ -effect is included, with a best estimate of  $\Lambda_i \sim 10^2$ . The corresponding Lorentz to Coriolis force ratio then spans the range  $10^{-3} \lesssim \Lambda_d^* \lesssim 10^7$ , with  $\Lambda_d^* \sim 0.1$  being the best estimate. Thus, barring the large uncertainties, the Lorentz force is predicted to be sub-dominant, but not negligible, in Jupiter's core.

Starchenko and Jones (2002) predict similar flow speeds for the Saturnian interior, which corresponds to a lower  $Rm \sim 10^4$  value due to the smaller size of the dynamo region. Saturn's magnetic field is also weaker than that of Jupiter; the best estimate imposed Elsasser number is  $\Lambda_i \sim 1$  with a feasible range of  $10^{-2} \lesssim \Lambda_i \lesssim 10^6$ . In the most likely scenario, the Lorentz force is predicted to be two orders of magnitude smaller than the Coriolis force ( $\Lambda_d^* \sim 10^{-2}$ ) with uncertainties extending the possible range to  $10^{-4} \lesssim \Lambda_d^* \lesssim 10^4$ .

**Ice Giants:** Uranus and Neptune have relatively weak core magnetic fields with  $\Lambda_i \sim 10^{-4}$  based on spacecraft observations, but there are few constraints on the flow speeds. We, therefore, assume  $U \sim 10^{-3}$  m/s based on the other planetary estimates such that  $Rm \sim 10^2$  to give an upper bound of  $\Lambda_i \sim 1$  when the toroidal estimate is included. For these  $\Lambda_i$  estimates, the predicted Lorentz to Coriolis force ratio is always less than unity:  $10^{-5} \lesssim \Lambda_d^* \lesssim 10^{-1}$ . These results thus imply that the ice giants are not in magnetostrophic balance.

## Conclusions

The Lorentz to Coriolis force ratio is an important parameter for the dynamics of planetary cores since dynamos with dominant Coriolis forces at global scales are expected to be driven by fundamentally different archetypes of fluid motions than those with dominant (or co-dominant) Lorentz forces (Roberts and King 2013, Calkins et al. 2015). We hypothesize that a representative global estimate of the Lorentz to Coriolis force ratio can be predicted by  $\Lambda_d^* = 0.77\Lambda_i Rm^{-1/2}$ . An advantage of this formulation is that it depends on quantities that can be estimated for planetary cores (Table 3). Our results

suggest that the Earth's core is likely to be in magnetostrophic balance where the Lorentz and Coriolis forces are comparable. The Lorentz force may also be substantial in Jupiter's core, where it is predicted to be a factor of ten less than the Coriolis force. Magnetic fields become increasingly sub-dominant for the other planets: the Coriolis force is predicted to exceed the Lorentz force by at least two orders of magnitude within the cores of Saturn, Uranus/Neptune, Ganymede, and Mercury.

These conclusions are subject to large uncertainties, however. Core flow speeds are difficult to estimate, while total magnetic field strengths cannot be measured directly. The applicability of Eq. 18 for the Lorentz to Coriolis force ratio may also break down at extreme planetary core conditions that cannot be explored numerically or in the laboratory due to technological limitations. In order to mitigate these uncertainties, we have considered a range of possible core magnetic field strengths ( $\Lambda_i$ ) and included state-of-the-art simulations (Sheyko 2014; cf. Nataf and Schraeffer 2015).

## Abbreviations

MHD: Magnetohydrodynamics; RMS: Root mean square; SKA: Soderlund et al. (2012, 2014); S14: Sheyko 2014.

## Competing interests

The authors declare that they have no competing interests.

## Authors' contributions

KMS and JMA designed the study. KMS and AS carried out and analyzed the numerical simulations. All authors interpreted the data. All authors read and approved the final manuscript.

## Acknowledgements

The authors thank two anonymous referees for their thoughtful reviews, Hao Cao for helpful suggestions, and Wolfgang Bangerth for enlightening discussions at the 2014 Study of Earth's Deep Interior (SEDI) meeting in Kanagawa, Japan. KMS gratefully acknowledges travel grants from the Japanese Geophysical Union and the National Science Foundation to attend this symposium as well as research support from the National Science Foundation (grant AST-0909206). JMA acknowledges the support of the National Science Foundation Geophysics Program (grant EAR-1246861). Computational resources supporting this work were provided by the NASA High-End Computing (HEC) Program through the NASA Advanced Supercomputing (NAS) Division at Ames Research Center and by the Swiss National Supercomputing Centre (CSCS) under project ID s225. This is UTIG contribution 2858.

## Author details

<sup>1</sup>Institute for Geophysics, John A. & Katherine G. Jackson School of Geosciences, The University of Texas at Austin, J. J. Pickle Research Campus, Building 196 (ROC), 10100 Burnet Road (R2200), Austin, Texas, 78758-4445, USA. <sup>2</sup>Institut für Geophysik, ETH Zürich, NO H 11.2, Sonneggstrasse 5 8092 Zürich, LA59 Switzerland. <sup>3</sup>U.S. Global Development Lab, U.S. Agency for International Development, Washington, DC, 20004, USA. <sup>4</sup>Department of Earth, Planetary, and Space Sciences, University of California, Los Angeles, 595 Charles Young Drive East, Los Angeles, California, 90095-1567, USA.

Received: 1 April 2015 Accepted: 10 August 2015

Published online: 02 September 2015

## References

Aubert J, Aurnou JM, Wicht J (2008) The magnetic structure of convection-driven numerical dynamos. *Geophys J Int* 172:945–956

- Aubert J, Labrosse S, Poitou C (2009) Modelling the palaeo-evolution of the geodynamo. *Geophys J Int* 179:1414–1428
- Aubert J (2013) Flow throughout the Earth's core inverted from geomagnetic observations and numerical dynamo models. *Geophys J Int* 192:537–556
- Aurnou JM, Heimpel MH, Wicht J (2007) The effects of vigorous mixing in a convective model of zonal flow on the Ice Giants. *Icarus* 190:110–126
- Cao H, Aurnou JM, Wicht J, Dietrich W, Soderlund KM, Russell CT (2014) A dynamo explanation for Mercury's anomalous magnetic field. *Geophys Res Lett* 41(12):4127–4134
- Cardin P, Olson PL (1995) The influence of toroidal magnetic field on thermal convection in the core. *Earth Planet Sci Lett* 133:167–181
- Cardin P, Brito D, Jault D, Nataf HC, Masson JP (2002) Towards a rapidly rotating liquid sodium dynamo experiment. *Magnetohydrodynamics* 38:177–189
- Cheng JS, Stellmach S, Ribeiro A, Grannon A, King EM, Aurnou JM (2015) Laboratory-numerical models of rapidly rotating convection in planetary cores. *Geophys J Int* 201:1–17
- Christensen U. R, Wicht J (2007) Numerical Dynamo Simulations. In: Schubert G (ed). *Treatise on Geophysics, Core Dynamics*. Elsevier, Amsterdam Vol. 8. pp 245–282. Chap. 8
- Christensen UR (2015) Iron snow dynamo models for Ganymede. *Icarus* 247:248–259
- Dharmaraj G, Stanley S (2012) Effect of inner core conductivity on planetary dynamo models. *Phys Earth Planet Int* 212–213:1–9
- Dharmaraj G, Stanley S, Qu AC (2014) Scaling laws, force balances and dynamo generation mechanisms in numerical dynamo models: influence of boundary conditions. *Geophys J Int* 199:514–532
- Dormy E, Soward AM, Jones CA, Jault D, Cardin P (2004) The onset of thermal convection in rotating spherical shells. *J Fluid Mech* 501:43–70
- Dormy E (2014) Strong field spherical dynamos. [arXiv:1412.4090v1](https://arxiv.org/abs/1412.4090v1)
- Galloway DJ, Proctor MRE, Weiss NO (1978) Magnetic flux ropes and convection. *J Fluid Mech* 87:243–261
- Gilman PA (1977) Nonlinear dynamics of Boussinesq convection in a deep rotating spherical shell – I. *Geophys Astrophys Fluid Dyn* 8:93–135
- Gillet N, Jault D, Canet E, Fournier A (2010) Fast torsional waves and strong magnetic field within the Earth's core. *Nature* 465:74–77
- Grooms I, Julien K, Weiss JB, Knobloch E (2010) Model of convective Taylor columns in rotating Rayleigh-Bénard convection. *Phys Rev Lett* 104:224501
- Holme R (2007) Large-scale flow in the core. In: Schubert G (ed). *Treatise on Geophysics, Core Dynamics*. Elsevier, Amsterdam Vol. 8. pp 107–130. Chap. 4
- Jones CA, Soward AM, Mussa AI (2000) The onset of thermal convection in a rapidly rotating sphere. *J Fluid Mech* 405:157–179
- Jones CA (2014) A dynamo model of Jupiter's magnetic field. *Icarus* 241:148–159
- Julien K, Knobloch E, Werne J (1998) A new class of equations for rotationally constrained flows. *Theoret Comput Fluid Dynamics* 11:251–261
- Julien K, Rubio AM, Grooms I, Knobloch E (2012) Statistical and physical balances in low Rossby number Rayleigh-Bénard convection. *Geophys Astrophys Fluid Dyn* 106:392–428
- Kageyama A, Miyagoshi T, Sato T (2008) Formation of current coils in geodynamo simulations. *Nature* 454:1106–1108
- King EM, Aurnou JM (2015) Magnetostrophic balance as the optimal state for turbulent magnetoconvection. *Proc Natl Acad Sci* 112:990–994
- Le Bars M, Cebbron D, Le Gal P (2015) Flows driven by libration, precession, and tides. *Annu Rev Fluid Mech* 47:163–193
- Nataf H-C, Schaeffer N (2015) Turbulence in the core. In: Olson P, Schubert G (eds). *Treatise on Geophysics, 2nd ed., Core Dynamics*. Elsevier BV, Amsterdam Vol. 8. pp 161–181. Chap. 6
- Olson PL, Glatzmaier GA (1996) Magnetoconvection and thermal coupling of the Earth's core and mantle. *Philos Trans R Soc London Ser A* 354:1413–1424
- Olson PL, Christensen UR, Glatzmaier GA (1999) Numerical modeling of the geodynamo: Mechanisms of field generation and equilibration. *J Geophys Res* 104:10383–10404
- Ribeiro A, Fabre G, Guermond JL, Aurnou JM (2015) Canonical models of geophysical and astrophysical flows: Turbulent convection experiments in liquid metals. *Metals* 5:289–335
- Roberts PH (1968) On the thermal instability of a rotating-fluid sphere containing heat sources. *Philos Trans R Soc London Ser A* 264:93–117
- Roberts, PH (2007) Theory of the geodynamo. In: Schubert G (ed). *Treatise on Geophysics, Core Dynamics*. Elsevier, Amsterdam Vol. 8. pp 67–105. Chap. 3
- Roberts PH, King EM (2013) On the genesis of the Earth's magnetism. *Rep Prog Phys* 76(9):096801
- Schubert G, Soderlund KM (2011) Planetary magnetic fields: Observations and models. *Phys Earth Planet Int* 187:92–108
- Sheyko A (2014) Numerical investigations of rotating MHD in a spherical shell. Dissertation, ETH ZURICH
- Shimizu H, Koyama T, Utada H (1998) An observational constraint on the strength of the toroidal magnetic field at the CMB by time variation of submarine cable voltages. *Geophys Res Lett* 25:4023–4026
- Soderlund KM, King EM, Aurnou JM (2012) The influence of magnetic fields in planetary dynamo models. *Earth Planet Sci Lett* 333–334:9–20
- Soderlund KM, Heimpel MH, King EM, Aurnou JM (2013) Turbulent models of ice giant internal dynamics: Dynamos, heat transfer, and zonal flows. *Icarus* 224:97–113
- Soderlund KM, King EM, Aurnou JM (2014) Corrigendum to "The influence of magnetic fields in planetary dynamo models". *Earth Planet Sci Lett* 392:121–123
- Sprague M, Julien K, Knobloch E, Werne J (2006) Numerical simulation of an asymptotically reduced system for rotationally constrained convection. *J Fluid Mech* 551:141–174
- Sreenivasan B, Jones CA (2011) Helicity generation and subcritical behavior in rapidly rotating dynamos. *J Fluid Mech* 688:5–30
- Sreenivasan B, Sahoo S, Gaurav D (2014) The role of buoyancy in polarity reversals of the geodynamo. *Geophys J Int* 199:1698–1708
- Starichenko SV, Jones CA (2002) Typical velocities and magnetic field strengths in planetary interiors. *Icarus* 157:426–435
- Stellmach S, Lischper M, Julien K, Vasil GM, Cheng JS, Ribeiro A, King EM, Aurnou JM (2014) Approaching the asymptotic regime of rapidly rotating convection: Boundary layers versus interior dynamics. *Phys Rev Lett* 113:254501
- Tritton DJ (1998) *Physical Fluid Dynamics*. Oxford University Press, Oxford
- Wicht J (2002) Inner-core conductivity in numerical dynamo simulations. *Phys Earth Planet Int* 132:281–302
- Zhang K (1992) Spiraling columnar convection in rapidly rotating spherical fluid shells. *J Fluid Mech* 236:535–554
- Zhang K, Schubert G (2000) Magnetohydrodynamics in rapidly rotating spherical systems. *Annu Rev Fluid Mech* 32:409–443
- Calkins MA, Julien K, Tobias SM, Aurnou JM (2015) A multiscale dynamo model driven by quasi-geostrophic convection. *J Fluid Mech*. doi:10.1017/jfm.2015.464
- Nataf H-C, Schaeffer N (2015) Turbulence in the core. In: Olson P, Schubert G (eds). *Treatise on Geophysics, 2nd ed., Core Dynamics*. Elsevier BV, Amsterdam Vol. 8. pp 161–181. Chap. 6

**Submit your manuscript to a SpringerOpen® journal and benefit from:**

- Convenient online submission
- Rigorous peer review
- Immediate publication on acceptance
- Open access: articles freely available online
- High visibility within the field
- Retaining the copyright to your article

Submit your next manuscript at ► [springeropen.com](http://springeropen.com)